Wavelength-selective switch with direct few mode fiber integration

D. M. Marom,[1,*] J. Dunayevsky,[2] D. Sinefeld,[1] M. Blau,[1] R. Ryf,[3] N. K. Fontaine,[3] M. Montoliu,[3,4] S. Randel,[3] C. Liu,[3] B. Ercan,[3] M. Esmaeelpour,[3] S. Chandrasekhar,[3] A. H. Gnauck,[3] S. G. Leon-Saval,[5] J. Bland-Hawthorn,[5] J. R. Salazar-Gil,[5] Y. Sun,[6] L. Grüner-Nielsen,[7] and R. Lingle, Jr.[6]

[1]*Applied Physics Dept., Hebrew University, Jerusalem, Israel*
[2]*Oclaro Corp., Jerusalem, (at time of submission), Israel*
[3]*Bell Laboratories, Alcatel-Lucent, 791 Holmdel-Keyport Rd, Holmdel, NJ, 07733, USA*
[4]*Universitat Politecnica de Catalunya (ETSETB), Barcelona, Spain*
[5]*Institute of Photonics and Optical Science (IPOS), The University of Sydney, Australia*
[6]*OFS, 2000 Northeast Expressway, Norcross, GA 30071, USA*
[7]*OFS, Priorparken 680, 2605 Brondby, Denmark*
*danmarom@mail.huji.ac.il

Abstract: The first realization of a wavelength-selective switch (WSS) with direct integration of few mode fibers (FMF) is fully described. The free-space optics FMF-WSS dynamically steers spectral information-bearing beams containing three spatial modes from an input port to one of nine output ports using a phase spatial light modulator. Sources of mode dependent losses (MDL) are identified, analytically analyzed and experimentally confirmed on account of different modal sensitivities to fiber coupling in imperfect imaging and at spectral channel edges due to mode clipping. These performance impacting effects can be reduced by adhering to provided design guidelines, which scale in support of higher spatial mode counts. The effect on data transmission of cascaded passband filtering and MDL build-up is experimentally investigated in detail.

References and links

1. J. Hecht, *City of Light: The Story of Fiber Optics* (Oxford University Press, 1999).
2. R.-J. Essiambre and R. W. Tkach, "Capacity trends and limits of optical communication networks," Proc. IEEE **100**(5), 1035–1055 (2012).
3. D. J. Richardson, J. Fini, and L. E. Nelson, "Space-division multiplexing in optical fibres," Nat. Photonics **7**(5), 354–362 (2013).
4. G. Li, N. Bai, N. Zhao, and C. Xia, "Space-division multiplexing: the next frontier in optical communication," Adv. Opt. Photon. **6**(4), 413–487 (2014).
5. D. M. Marom, D. T. Neilson, D. S. Greywall, C. S. Pai, N. R. Basavanhally, V. A. Aksyuk, D. O. López, F. Pardo, M. E. Simon, Y. Low, P. Kolodner, and C. A. Bolle, "Wavelength-selective 1×K switches using free-space optics and MEMS micromirrors: theory, design, and implementation," J. Lightwave Technol. **23**(4), 1620–1630 (2005).
6. M. D. Feuer, D. C. Kilper, and S. L. Woodward, "ROADMs and their system applications," in *Optical Fiber Telecommunications,* V-B, I.P. Kaminow, T. Li, and A. Willner, eds. (Academic Press, 2008), Ch. 9.
7. L. E. Nelson, M. D. Feuer, K. Abedin, X. Zhou, T. F. Taunay, J. M. Fini, B. Zhu, R. Isaac, R. Harel, G. Cohen, and D. M. Marom, "Spatial superchannel routing in a two-span ROADM system for space division multiplexing," J. Lightwave Technol. **32**(4), 783–789 (2014).
8. J. Carpenter, S. G. Leon-Saval, J. R. Salazar-Gil, J. Bland-Hawthorn, G. Baxter, L. Stewart, S. Frisken, M. A. F. Roelens, B. J. Eggleton, and J. Schröder, "1x11 few-mode fiber wavelength selective switch using photonic lanterns," Opt. Express **22**(3), 2216–2221 (2014).
9. N. K. Fontaine, R. Ryf, C. Liu, B. Ercan, J. R. Salazar Gil, S. G. Leon-Saval, J. Bland-Hawthorn, and D. T. Neilson, "Few-mode fiber wavelength selective switch with spatial-diversity and reduced-steering angle," Proc. Opt. Fiber Commun. (OFC) 2014, San Francisco, CA. Paper Th4A.7.
10. R. Ryf, N. K. Fontaine, J. Dunayevsky, D. Sinefeld, M. Blau, M. Montoliu, S. Randel, C. Liu, B. Ercan, M. Esmaeelpour, S. Chandrasekhar, A. H. Gnauck, S. G. Leon-Saval, J. Bland-Hawthorn, J. R. Salazar-Gil, Y. Sun, L. Gruner-Nielsen, R. Lingle, Jr., and D. M. Marom, "Wavelength selective switch for few-mode fiber

transmission," Proc. European Conf. on Opt. Commun. (ECOC) 2013, London, UK. Post deadline paper PD1.C.4.
11. R. Y. Gu, E. Ip, M. Li, Y. Huang, and J. M. Kahn, "Experimental demonstration of a spatial light modulator few-mode fiber switch for space-division multiplexing," Proc. Frontiers in Opt. 2013, post deadline paper FW6B.4.
12. K.-P. Ho, J. M. Kahn, and J. P. Wilde, "Wavelength-selective switches for mode-division multiplexing: Scaling and performance analysis," J. Lightwave Technol. **32**(22), 3724–3735 (2014).
13. A. T. O'Neil and J. Courtial, "Mode transformations in terms of the constituent Hermite–Gaussian or Laguerre–Gaussian modes and the variable-phase mode converter," Opt. Commun. **181**(1–3), 35–45 (2000).
14. A. Yariv, *Optical Electronics*, 4th ed. (Saunders College Publishing, 1991), Chap. 2.
15. S. Chandrasekhar, X. Liu, B. Zhu, and D. W. Peckham, "Transmission of a 1.2-Tb/s 24-carrier no-guard-interval CO-OFDM superchannel over 7200-km of ultra-large-area fiber," Proc. European Conf. on Opt. Commun. (ECOC) 2009, Vienna, Austria. Post deadline paper PD2.6.
16. N. K. Fontaine, R. Ryf, M. A. Mestre, B. Guan, X. Palou, S. Randel, Y. Sun, L. Grüner-Nielsen, R. V. Jensen, and R. Lingle Jr., "Characterization of space-division multiplexing systems using a swept-wavelength interferometer," Proc. Opt. Fiber Commun. (OFC) 2013, Anaheim, CA. Paper OW1K.2.
17. R. Ryf, M. A. Mestre, A. Gnauck, S. Randel, C. Schmidt, R. Essiambre, P. Winzer, R. Delbue, P. Pupalaikis, A. Sureka, Y. Sun, X. Jiang, D. Peckham, A. H. McCurdy, and R. Lingle, "Low-loss mode coupler for mode-multiplexed transmission in few-mode fiber," Proc. Opt. Fiber Commun. (OFC) 2012, Los Angeles, CA. Post deadline paper PDP5B.5.
18. D. Sinefeld and D. M. Marom, "Insertion loss and crosstalk analysis of a fiber switch based on a pixelized phase modulator," J. Lightwave Technol. **29**(1), 69–77 (2011).
19. S. Randel, R. Ryf, A. Gnauck, M. A. Mestre, C. Schmidt, R. Essiambre, P. Winzer, R. Delbue, P. Pupalaikis, A. Sureka, Y. Sun, X. Jiang, and R. Lingle, "Mode-multiplexed 6×20-GBd QPSK transmission over 1200-km DGD-compensated few-mode fiber," Proc. Opt. Fiber Commun. (OFC) 2012, Los Angeles, CA. Post deadline paper PDP5C.5.
20. N. K. Fontaine, R. Ryf, J. Bland-Hawthorn, and S. G. Leon-Saval, "Geometric requirements for photonic lanterns in space division multiplexing," Opt. Express **20**(24), 27123–27132 (2012).
21. S. G. Leon-Saval, A. Argyros, and J. Bland-Hawthorn, "Photonic lanterns: a study of light propagation in multimode to single-mode converters," Opt. Express **18**(8), 8430–8439 (2010).
22. J. von Hoyningen-Huene, R. Ryf, and P. Winzer, "LCoS-based mode shaper for few-mode fiber," Opt. Express **21**(15), 18097–18110 (2013).

1. Introduction

Optical communication networks based on the ubiquitous single mode fiber (SMF) have supported the exponentially growing information demand since its introduction in the 1980's [1]. The capacity transmitted over a single SMF has grown steadily based on innovations such as wavelength-division multiplexing (WDM), polarization multiplexing (PolMux), and multi-level signaling with coherent detection. Now that these degrees of freedom have been exhausted and the information demand continues to grow unabated, the spatial mode domain is being actively investigated for providing future capacity growth avenues [2]. In the last few years many fiber designs supporting several spatial modes have been introduced, which are broadly categorized as multi-core fibers (MCFs) and few-mode fibers (FMFs) [3]. These fibers will enable space-division multiplexing (SDM) to be employed in the future and provide the additional capacity required to deliver data at a decreasing cost per bit [4]. Yet alongside the new fibers being considered for SDM, the ancillary components required to realize complete optical communication networks have to be updated for SDM compatibility.

Wavelength-selective switches (WSSs) are a key component in today's SMF based optical networks. A WSS has a single input port and multiple output ports to which WDM channels are independently routed [5]. They are used individually as a programmable multiplexer or demultiplexer at network ingress and egress points, in pairs to realize a reconfigurable optical add/drop multiplexer (ROADM), and as a modular switching element in mesh network nodes [6]. Hence, it is imperative that WSS functionality be expanded to support SDM-based optical networks. The simplest method to introduce SDM to the WSS is by placing mode demultiplexers that separate the fiber modes to individual single mode channels that interface to the WSS (typically one configured for high port counts) [7]. Since within the WSS all ports are imaged onto each other at the spectrally dispersed plane (which is why a conventional WSS can only operate with a single input port), introducing several spatial channels in parallel to the WSS allows only '*joint switching*' of WDM channels which means that all the spatial modes are switched together from the set of input ports assigned to the input SDM link to a set of output ports assigned to an output SDM fiber link. The joint switching functionality is

actually a necessary requirement for SDM links that experience mode mixing, hence this is not seen as an impediment in most cases. The joint switching WSS was first demonstrated with a seven-core MCF interfaced with mode demultiplexers to a commercial 21-port count WSS to realize a 7 × (1 × 2) switching functionality [7]. Similar joint switching WSS with interfaces to FMF were subsequently implemented, with either external demultiplexers attached to a commercial WSS [8] or internal demultiplexers introduced into the WSS fabric [9]. However, the operations of mode demultiplexing and multiplexing before and after every SDM-modified WSS incurs excess loss which inevitably leads to reduced transmission range. In addition, the WSS addressable port count is decreased by the SDM factor, reducing switching functionality. Hence, it is highly desired to integrate the SDM fiber directly into the WSS and provide a low-loss, high port count switch.

In this paper we expand on the report of the first realization of a 1 × 9 WSS with direct integration of three mode fiber [10]. Other realizations have since been reported [11] and analyzed [12]. The optical design of our FMF-WSS, the source of mode dependent loss (MDL) and its increased sensitivity for multi-mode beams is identified. The MDL at the channel transition from pass to block band is explained and identified as the limiting factor in determining the channel's useable bandwidth. The WSS analysis presented here is different than the one of [12] and more detailed, whereas [12] focuses more on switch scaling. Finally, data transmission experiments demonstrate the usefulness of the FMF-WSS for carrying SDM data through many network switching nodes.

2. FMF-WSS optical design

SMF-WSS typically employ free-space optics to disperse and switch WDM channels from the input port to one of the possible output ports. In a standard system configuration (see Fig. 1(left)), a Gaussian beam emerging from the ingress SMF port is collimated by a mating micro-lens such that the collimated beam waist is projected onto a diffraction grating. Anamorphic beam expansion may advantageously be incorporated to illuminate a larger number of grooves of the diffraction grating, for obtaining greater spectral resolving power without increasing total system height, as well as a polarization diversity solution to eliminate polarization dependent losses (PDL). The beam then experiences angular dispersion upon diffraction, which is mapped to spatial dispersion with a Fourier lens. At the lens's front focal plane the switching action occurs by beam steering, with either tilting MEMS micromirrors or liquid-crystal based phase-only spatial light modulation (SLM), in channelized form for independently addressing each WDM channel. This switching occurs at the central plane of symmetry of the optical arrangement, and ideally where the Gaussian beam waist should again emerge, for efficient coupling back into the output fibers. Indeed, if the Gaussian waist is successfully projected on the diffraction grating, it will also be placed at the switching plane due to the Fourier transform relationship between the lens's front and back focal planes.
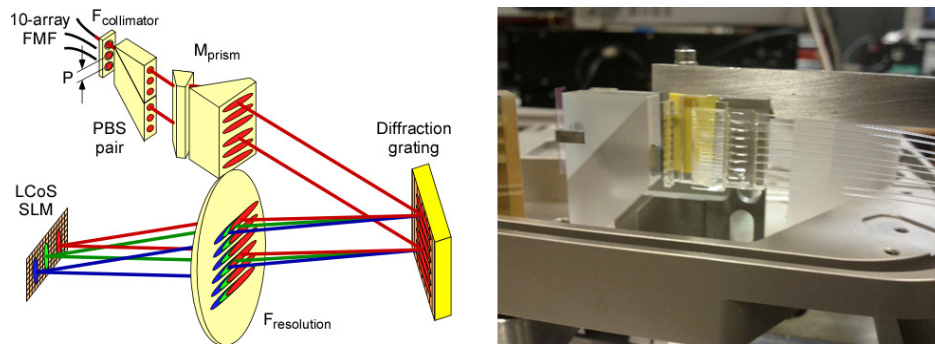

Fig. 1. Left: Optical design of the WSS, including anamorphic optics and polarization diversity. Right: Picture of the FMF held in V-groove adjacent to the microlens array used for collimation.

In this work we utilize the optical design of a commercial WSS, operating along the principle described above, and replace the input/output SMF array with a FMF array, where each fiber of the array supports two mode groups, or three spatial modes: LP_{01} and the doubly-degenerate LP_{11}. The beams emerging from the FMF are propagated in free-space, traversing the various optical elements of the WSS (e.g., lenses, diffraction grating, anamorphic optics, and beam-steering element) before coupling back into the output fibers. When treating free-space beams emerging from SMF, it is customary to approximate the fundamental Bessel mode (of type J/K in core/cladding) with a continuous Gaussian beam. The rules of propagation for Gaussian beams in free-space are well developed. In an analogous manner, we approximate the modes of the FMF to Hermite-Gaussian (HG) beams, which like the Gaussian beam are shape-preserving solutions of free-space propagation under the paraxial approximation (the Helmholtz equation) in Cartesian coordinate system and uniform refractive index medium. Fiber modes are typically approximated by Laguerre-Gaussian (LG) beams, which are defined in a cylindrical coordinate system that is more conducive to the fiber geometry and the LG subscripts relate directly to the azimuthal and radial orders, also used in linearly polarized (LP) mode designation. The HG and LG basis expansions can be converted to each other with known mappings [13]. The fundamental mode group, LP_{01}, is approximated by HG_{00}, and the degenerate LP_{11} mode group by HG_{01} and HG_{10}. The degenerate LP_{21} mode group is approximated by HG_{11} and HG_{02}-HG_{20}, whereas the LP_{02} group by $HG_{02} + HG_{20}$ (here we witness that the LP modes are not directly related to the HG modes but to a linear combination of them). We prefer the HG basis expansion in a Cartesian coordinate system for beam modeling within the WSS since the optical beams will be stretched in one dimension by the anamorphic effects of prisms and the grating, hence forming elliptical modes which are not supported by circularly symmetric LG beams. Furthermore, the beams will be dispersed along one spatial dimension and switched along channel boundaries further defined in one dimension, making the separable Cartesian representation more natural for the WSS evaluation. An HG beam propagating in free-space evolves according to [14]:

$$
\begin{aligned}
E_{m,n}\left(x, \mathrm{y}, z\right) = A_{m,n} \frac{w_0}{w(z)} H_m\left(\sqrt{2}\,\frac{x}{w(z)}\right) H_n\left(\sqrt{2}\,\frac{y}{w(z)}\right) \\
\cdot \exp\left(-\frac{x^2 + y^2}{w^2(z)} - j\frac{k\left(x^2 + y^2\right)}{2R(z)} - jkz + j\left(m+n+1\right)\tan^{-1}\left(\frac{z}{z_0}\right)\right)
\end{aligned}
\tag{1}
$$

where the Rayleigh range, z_0, waist parameter, $w(z)$, and radius of curvature, $R(z)$, are all defined exactly in accordance to the Gaussian beam definition, and $H_m(\bullet)$ is the m'th order Hermite polynomial. While the HG beam has a Gaussian apodization function, it is broadened along a Cartesian coordinate by the order of the Hermite polynomial associated with the coordinate. The HG beam size, defined by the full width at $\exp(-2)$ level of the maximum intensity along the x-coordinate is well approximated by the expression:

$$
\mathrm{BeamSize} = 2\sqrt{1 + 1.2m - 0.0125m^2} \cdot w(z)
\tag{2}
$$

(for the fundamental Gaussian beam, $m = 0$, the expression reduces to a beam width of $2w(z)$, and $2w_0$ at the waist). The increased size of higher order HG beams is significant in determining beam clipping at finite apertures (in the WSS case, the fiber collimator lenses) and at spectral channel boundaries at the switching plane. Since the field curvature of the beam is independent of the HG order, all orders obey the same propagation and focusing properties as the fundamental Gaussian beam, and hence all fiber modes can co-propagate as HG beams in free-space and focus at common planes.

The FMF was placed in a V-groove holder with a 1.25 mm pitch, matching that of the collimator array (see Fig. 1(right)). A microlens array of focal length 3.875 mm and the same

pitch is used in attempt to collimate the beams and project the waist a distance of ~125 mm onto the diffraction grating (sufficient distance for placing polarization diversity and anamorphic optics elements between the collimator and grating). The fiber-collimator distance determines the waist formation location and size (Fig. 2(A)) and enables to project the waist to the grating when the fiber source is SMF with 10.5 μm mode size. However, the FMF we used to construct the FMF-WSS (OFS, model: two mode step-index fiber) had a low numerical aperture of 0.11, from which we calculate that the guided beams have a waist size of 16.5 μm. While the lower divergence of the FMF's greater mode size allows the microlens aperture to pass the LP11 mode without clipping (the aperture was originally designed to pass the fundamental mode emerging from a SMF source), it further implies that the waist cannot be projected to the full distance of the grating (see Fig. 2(B)). We set the fiber-collimator distance to achieve a maximum waist 'throw,' at about $v = 55$ mm, which is shorter than the distance to the grating, and thus a field curvature is present on the beam striking the grating at the lens back focal plane.
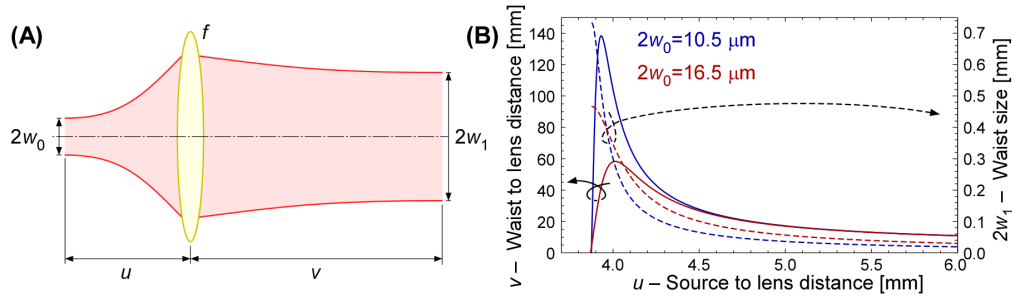

Fig. 2. Gaussian beam collimation with a lens. (A) Gaussian beam with waist of size $2w_0$ placed a distance u from lens f projects the waist of new size $2w_1$ to a distance v beyond the lens. (B) Evaluation of waist formation conditions (projection distance, v, solid lines; formed beam size, $2w_1$, dashed lines) for two different input Gaussian beam sizes with an $f = 3.875$ mm lens.

To assess the system impact of the shorter waist projection distance, we track the fundamental Gaussian waist parameter, $w(z)$, through the WSS as it traverses the different optical elements. This is done independently for the beam height (y-direction), which is along the fiber port direction (Fig. 3(top)), and the beam width (x-direction), which is along the wavelength-dispersion direction (Fig. 3(bottom)). We plot the beam evolution for the originally designed specification (with SMF, traced in blue) and the larger mode size of the FMF (traced in maroon). With SMF inputs, the waist is properly located on the diffraction grating (its locations designated by the dashed green line, roughly at 125 mm for separating spectral components and at 725 mm on the return path for combining spectral components) and at the spectral switching plane (designated by black line at 425 mm). With our FMF and collimator, the waist evolution is not symmetric about the spectral switching plane, and the beam arriving back to the output fiber is not focused at the fiber plane and is not properly sized. A zoomed in view of the output fiber plane (Fig. 3(right)) shows the SMF beam (blue) focused to a 10.5 μm spot exactly on the fiber plane, whereas the FMF beam (maroon) focuses farther and to smaller spot sizes than the 16.5 μm specification. The focused spot size and location imperfections are different in the port and wavelength directions. These imperfections will lead to fiber coupling losses, which have to be computed for every supported fiber mode.
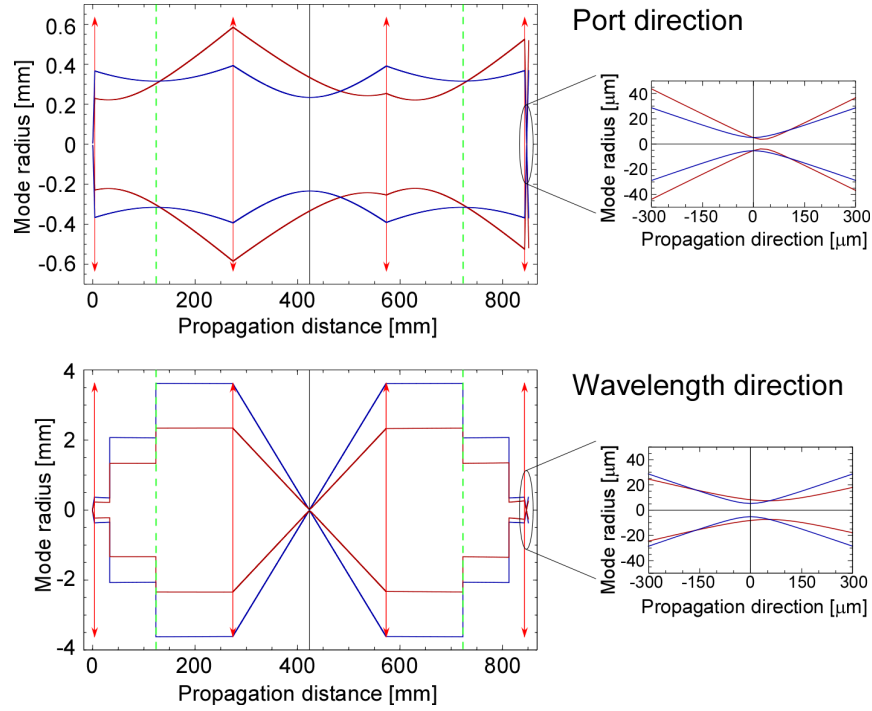
Fig. 3. Waist size evolution as the beam traverses the WSS, plotted for SMF in blue (10.5 μm beam size source) and employed FMF in maroon (16.5 μm beam size source). Top: Beam height (*y*-direction), which is along the fiber port direction. Bottom: Beam width (*x*-direction), which is along the wavelength-dispersion direction. Right: Zoom in on the output plane, where the beam arrives to the output fiber. Lenses shown as vertical red lines with arrows, diffraction gratings as vertical dashed green lines, and the symmetry plane where the spectral components are separated in a vertical black line. Beam size is expanding in discrete jumps in wavelength direction by anamorphic prisms and anamorphic effect at diffraction grating.
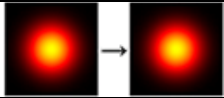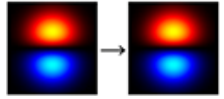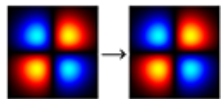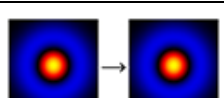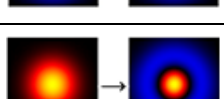
At the output fiber facet position, the incident HG beam parameters deviate from the ideal parameters (beam size and longitudinal waist position) required for efficient power coupling due to the limited waist projection distance. The geometric ray tracing throughout the WSS is not impacted by the HG beam waist evolution, and hence the beam is incident onto the output fibers with no angular offset (normal incidence) and no transverse offset. With the HG beam approximation we analytically calculate the fiber coupling efficiency as a function of beam size at the waist location and the longitudinal offset of the waist position to the fiber facet, ΔL. The fiber coupling efficiency is defined by

$$\eta = \frac{\iint E_{mn} E'_{rs} dxdy}{\sqrt{\iint |E_{mn}|^2 \, dxdy} \cdot \sqrt{\iint |E_{rs}|^2 \, dxdy}} \qquad (3)$$

where E_{mn} is the HG fiber mode and E'_{rs} is the HG incident beam, with the tag denoting the beam is possibly improperly sized and placed. The HG beam indices of the investigated fiber mode and incident beam do not have to be the same, so modal crosstalk can also be investigated. Since the HG modes are orthogonal to each other, the crosstalk would be zero with no imperfections (mode size matched and properly focused). We calculated the fiber coupling power efficiencies (i.e., $|\eta|^2$) for the first four spatial modes (LP$_{01}$, LP$_{11}$, LP$_{21}$, and LP$_{02}$) as presented in Table 1 (note we only have LP$_{01}$ and LP$_{11}$ in our WSS system). The HG beam size is captured by the beam's Rayleigh distance ($z_0 = \pi w_0^2 / \lambda$) in the developed expressions. Unsurprisingly, modal crosstalk under beam size mismatches and longitudinal

offsets can only occur between modes with matching azimuthal orders due to the symmetries involved (in our case, only LP$_{01}$ and LP$_{02}$ can cross-couple). What we learn is that the higher order spatial modes are much more sensitive to beam size mismatches and/or longitudinal offsets. Hence while all HG beams will focus to the same position and with the same waist size parameter, $2w_0$, the fiber coupling efficiency is strongly mode dependent and hence will lead to MDL.

Table 1. Fiber-coupling power efficiency per mode pairs as function of mode-size mismatch and longitudinal offset for first four fiber LP modes. Degenerate modes (e.g., LP$_{11}^a$ and LP$_{11}^b$) behave identically and do not cross-couple under these conditions.

Fiber mode	HG beam	Fiber-coupling power efficiency
LP$_{01}$→LP$_{01}$		$\dfrac{4z_0 z_1}{\left(z_0 + z_1\right)^2 + \left(\Delta L\right)^2}$
LP$_{11}$→LP$_{11}$		$\dfrac{\left(4z_0 z_1\right)^2}{\left(\left(z_0 + z_1\right)^2 + \left(\Delta L\right)^2\right)^2}$
LP$_{21}$→LP$_{21}$		$\dfrac{\left(4z_0 z_1\right)^3}{\left(\left(z_0 + z_1\right)^2 + \left(\Delta L\right)^2\right)^3}$
LP$_{02}$→LP$_{02}$		$\dfrac{4z_0 z_1\left(6z_0 z_1 - z_0^2 - z_1^2 - \left(\Delta L\right)^2\right)^2}{\left(\left(z_0 + z_1\right)^2 + \left(\Delta L\right)^2\right)^3}$
LP$_{01}$→LP$_{02}$		$\dfrac{4z_0 z_1\left(\left(z_0 - z_1\right)^2 + \left(\Delta L\right)^2\right)}{\left(\left(z_0 + z_1\right)^2 + \left(\Delta L\right)^2\right)^2}$
Other modal crosstalk		0

3. FMF-WSS construction and characterization

After setting the beam collimation condition between the FMF array and microlens array, the entire WSS was constructed. An anamorphic prism pair and polarization diversity optics were placed in the collimated beam path before striking a 1200 gr/mm reflection grating at 75° angle of incidence. The diffracted beam experiences angular dispersion of 20.76 mrad/THz, which is converted by an f = 150 mm Fourier lens to spatial dispersion of dx/dv = 3.115 µm/GHz at the spectral switching plane. We used a liquid-crystal on silicon (LCoS), phase only, HDTV standard SLM at the switching plane to flexibly select the WDM channel boundaries. The entire conventional band (C-band) of optical communications (1530-1560nm) is dispersed along the long axis of the SLM. The spot size, $2w_0$, at the Fourier plane in the spatial dispersion direction as evaluated from the simulation results of Fig. 3 is ~63 µm. This represents the full beam width for the fundamental Gaussian mode (LP$_{01}$), which expands to ~93 µm for the second spatial mode's full beam width (LP$_{11}$, by substituting m = 1 in Eq. (2)). The beam width at the Fourier plane is significant as it determines the transition bandwidth of a filtering edge (i.e., the roll-off between pass and block band), which is found by the ratio of the beam size to the spatial dispersion. For the fundamental mode (LP$_{01}$), this transition bandwidth is 20.2 GHz, and for the LP$_{11}$ the transition bandwidth increases to 29.9 GHz. The implication of this is that for a selected channel bandwidth, the pass bandwidth (characterized by flat low-IL) will be narrower for the higher order modes.
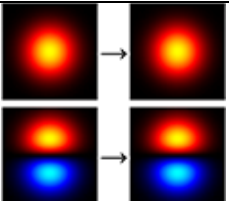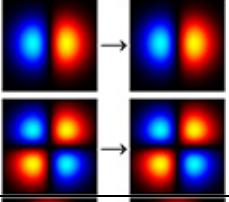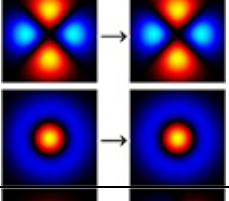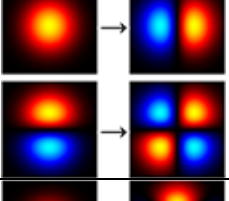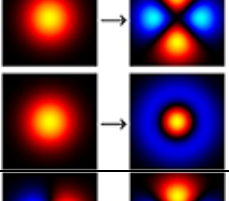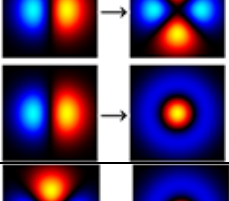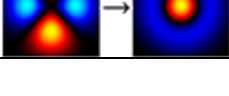
While the selection of channel bandwidth at the spectrally dispersed plane results in flat pass bandwidth for the frequency components whose spatial modes are fully contained within

the spatially defined region, other frequency components whose spatial modes extend to the channel edge inevitable suffer clipping. As the frequency components extend further to the channel boundary region, this clipping is exacerbated resulting in a roll-off from the pass-band to the block-band. Due to the different spatial mode structures, this roll-off will be strongly mode-dependent. Moreover, spatial modes lose their orthogonality when spatially clipped giving rise to mode mixing. This mode mixing becomes frequency dependent due to the spatial dispersion, which may be more challenging to overcome in receiver DSP. Using the HG beam formulation, we can calculate the mode dependent fiber coupling by solving the overlap integral at the spectrally dispersed plane. Here we modify Eq. (3) to take into account the frequency-dependent location of the HG mode and the finite integration range over the selected channel boundaries (width of $\Delta x = \Delta v \cdot dx/dv$ to select bandwidth of Δv about position x_0, where the channel center frequency v_0 strikes) across all mode combinations:

$$\eta(v) = \frac{\int_{x_0-\Delta x/2}^{x_0+\Delta x/2} \int_{-\infty}^{\infty} E_{mn}\left(x - (v - v_0)\frac{dx}{dv}, y\right) E'_{rs}\left(x - (v - v_0)\frac{dx}{dv}, y\right) dydx}{\sqrt{\iint |E_{mn}|^2 \, dxdy} \cdot \sqrt{\iint |E_{rs}|^2 \, dxdy}} \quad (4)$$

Here the Cartesian support of the HG beams comes strongly into play, as the y-axis dependence, which is integrated over its entire range, can be factored out as HG beams are separable. We solve Eq. (4) for a single channel edge, as typically the channel bandwidth selection width, Δx, is much wider than the mode sizes and the two edges do not contribute simultaneously (a requirement for getting flat, low-loss passband). The fiber-coupled efficiency (note, not fiber coupled power efficiency) for the first four spatial modes (LP_{01}, LP_{11}, LP_{21}, and LP_{02}) and their crosstalk combinations is provided in Table 2, with x_0 denoting the clipping edge location with respect to the center of the mode ($x_0 = 0$ implies clipping edge is at the mode's center; for each spectral component the clipping edge strikes at a different displacement from mode center). In these derivations we use the complementary error function, $\operatorname{erfc}(x) \triangleq 2/\sqrt{\pi} \cdot \int_x^{\infty} \exp(-t^2)dt$, and the incomplete Gamma function, $\Gamma(a,x) \triangleq \int_x^{\infty} t^{a-1} \exp(-t)dt$. Modal power attenuation and crosstalk at the channel edge region as a function of frequency is depicted in Fig. 4(left) for our system parameters.

Table 2. Fiber-coupling power efficiency per mode pairs as function of mode-size edge clipping for first four fiber LP modes

| Fiber mode	HG beam	Fiber-coupling efficiency
$LP_{01} \rightarrow LP_{01}$ $LP_{11}^a \rightarrow LP_{11}^a$		$\dfrac{1}{2}\mathrm{erfc}\left[\sqrt{2}\,\dfrac{x_0}{w_0}\right]$
$LP_{11}^b \rightarrow LP_{11}^b$ $LP_{21}^a \rightarrow LP_{21}^a$		$\sqrt{\dfrac{2}{\pi}}\,\dfrac{x_0}{w_0}\exp\left[-\dfrac{2x_0^2}{w_0^2}\right]+\dfrac{1}{2}\mathrm{erfc}\left[\sqrt{2}\,\dfrac{x_0}{w_0}\right]$
$LP_{21}^b \rightarrow LP_{21}^b$ $LP_{02} \rightarrow LP_{02}$		$\dfrac{3}{8}\mathrm{erfc}\left[\sqrt{2}\,\dfrac{x_0}{w_0}\right]-$ $\dfrac{1}{2\sqrt{\pi}}\left(\Gamma\left[\dfrac{3}{2},2\dfrac{x_0^2}{w_0^2}\right]-\Gamma\left[\dfrac{5}{2},2\dfrac{x_0^2}{w_0^2}\right]\right)$
$LP_{01} \rightarrow LP_{11}^b$ $LP_{11}^a \rightarrow LP_{21}^a$		$\dfrac{1}{\sqrt{2\pi}}\exp\left[-\dfrac{2x_0^2}{w_0^2}\right]$
$LP_{01} \rightarrow LP_{21}^b$ $LP_{01} \rightarrow LP_{02}$		$\dfrac{1}{\sqrt{2\pi}}\,\dfrac{x_0}{w_0}\exp\left[-\dfrac{2x_0^2}{w_0^2}\right]$
$LP_{11}^b \rightarrow LP_{21}^b$ $LP_{11}^b \rightarrow LP_{02}$		$\dfrac{1}{2\sqrt{2\pi}}\left(1+\dfrac{4x_0^2}{w_0^2}\right)\exp\left[-\dfrac{2x_0^2}{w_0^2}\right]$
$LP_{21}^b \rightarrow LP_{02}$		$\dfrac{1}{2\sqrt{2\pi}}\,\dfrac{x_0}{w_0}\left(1+\dfrac{4x_0^2}{w_0^2}\right)\exp\left[-\dfrac{2x_0^2}{w_0^2}\right]$
Other modal crosstalk		0
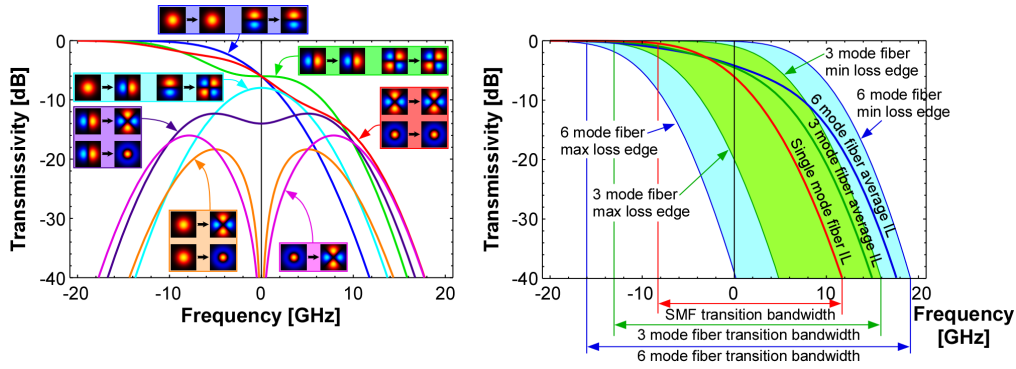
Fig. 4. Mode dependent transitions at channel edge with edge placed at 0 frequency. Left: per-mode fiber coupled power and modal crosstalk due to spatial mode clipping at physical edge of spectral filter. Frequency dependence is introduced by spatially dispersed mode positions. Right: Comparison of channel edge transitions for single mode, three mode and six mode fibers by eigenvalue analysis. In few mode case, the transition can fluctuate between the minimum and maximum loss edges, depending on the actual instantaneous mode excitation values (data dependent), causing further broadening of the transition bandwidth between pass and block.

The mode coupling values are inserted into a square coupling matrix (dimension being equal to the spatial mode count), which defines the fiber coupling and mode mixing values between the input and output mode sets. Since the LP modes are real (positive and negative amplitude values only), so are the fiber coupling and matrix values. From the coupling matrix's eigenvalues squared we find the power efficiency of the system's eigenmodes. Their average and extreme values are plotted in Fig. 4(right), for a three mode fiber (our experimental case), six mode fiber, and compared to a single mode fiber (the latter has a single eigenmode and is defined by a single curve [5]). The transition from passband to stopband determines the guard bandwidth required between adjacent WDM channels in order for them to be switched by network WSS without incurring spectral filtering or channel crosstalk that will impact the signal quality. In the SMF case, the passband ends when the transition reaches −0.5 dB and the blockband starts when the attenuation reaches −40 dB. The transition from −0.5 dB down to −40 dB is determined by the Gaussian power clipping function, i.e. $\left(\mathrm{erfc}\left[\sqrt{2}\cdot x_0/w_0\right]/2\right)^2$ according to Table 2, which occupies a physical width of $\sim 2w_0$. This physical width is converted to frequency by the spatial dispersion term, which for our spot size and dispersion results in a 20.2 GHz guard band, as estimated earlier. In the few-mode fiber case, the eigenvalues determine a transition zone that is no longer specified by a single curve (e.g. the average IL), but rather by a region bound by the maximum and minimum eigenvalue powers. The reason for the undeterministic behavior is that the actual light distribution is time varying and dependent on the modal content. There is a finite probability that the instantaneous modal content will exactly match one of the system's eigenvectors, which can lead in one extreme case to a transition curve bound by the smallest eigenvalue (the max-loss edge) and in the other extreme case to a transition bound by the largest eigenvalue (the min-loss edge). Hence in order to broadly define the necessary guard band in the FMF case, the passband ends when the maximum loss curve reaches −0.5 dB and the blockband begins when the minimum loss curve reaches −40 dB. Using the coupling matrix eigenvalue analysis and its plot (Fig. 4(right)), we find the guard transition extends over 29.5 GHz for the three mode case, in line again with our estimate based on the LP_{11} mode beam size. Similarly, we can extend the analysis to the six mode case. Here the LP_{02} full width will be 83% larger than the fundamental mode (according to Eq. (2) with $m = 2$), hence 115 μm, and lead to a guard band transition of 37 GHz, which closely matches the min-max eigenvalue curve spread (predicting ~36 GHz).

The broader transition bandwidth is an inherent attribute of a WSS with direct FMF interfaces. However, since the transition scales with the optical resolution of the dispersive

optical arrangement of the WSS, it can be addressed by designing the WSS to have greater resolving power, by either decreasing the spot size in the spectral plane or increasing the spatial dispersion. Alternatively, the wasted bandwidth on inter-WDM channel guard bands can be minimized by utilizing spectrally wide super-channels [15] that are composed of multi-carrier signals that are jointly routed through the optical network. Having fewer, broader WDM super-channels to route within the optical communication band will decrease the relative inefficiency of larger guard bands.

The optical characterization of the FMF-WSS was performed using a swept-wavelength interferometer, which is a well-established characterization technique for SMF-based devices that was recently extended to support few-mode fiber [16]. The measurement provides the full characterization of the device under test including phase and amplitude of transmission spectra for all input-output combinations of the multi-port device, which are assembled in a matrix (of dimension 6×6 in our case, as we have three spatial modes each supporting two orthogonal polarization states). From the matrix eigenvalues we can extract all the relevant system metrics as average insertion loss (IL), mode dependent loss (MDL), wavelength dispersion, and modal dispersion. The interferometer is divided to parallel SMF branches that are multiplexed in and out of the FMF using a 3D-waveguide based 3-spot coupler (3DW-MUX) [17]. (The 3DW-MUX incorporated depressed-cladding fiber with an LP_{01} effective area of 155-μm^2, which was attached via physical contact connectors to the step index FMF of the WSS with its 215-μm^2 effective area fiber. This mode size mismatch is an additional source of MDL, per the calculations of Table 1).

The first WSS characterization experiment consists of encoding the LCoS SLM with a single flexible channel definition, varying the selected bandwidth from 25 GHz to 150 GHz in 25 GHz increments. For the 100 and 50 GHz cases we plot the six eigenvalue power values as a function of frequency offset (thin lines in Fig. 5(A)–5(B)). Within the passband, where the HG modes are contained within the selected region, we observe no spectral fluctuation in eigenvalues. At the channel transition the power rapidly drops with a spectral spread of the transition point. We average the eigenvalue power values to obtain the mode-averaged IL (shown in thick line) and the difference between the strongest and weakest eigenvalue power defines the MDL (red line). As expected, the bandwidth defined by the MDL curve is narrower than the average IL curve, thus restricting the transmission bandwidth. For example, at the 100 GHz channel bandwidth definition, the −3dB bandwidth is 96 GHz using the average IL curve and reduces to 84 GHz using the MDL curve. While the eigenvalues do not necessarily correspond one-to-one to the fiber modes, we clearly observe within the passband region two better performing states to the remaining four (with about a 3 dB gap between the two groups). We attribute the two better performing eigenvalues to the LP_{01} mode, and the four worse performing ones to the LP_{11} mode. We expect worse performance for the LP_{11} mode due to the improper waist projection within the WSS, which returns the beams to the output fiber with a focusing error that impacts the higher order modes more severely. The average IL and MDL for the six flexibly defined channel bandwidths is shown in Fig. 5(C). The transition shape looks identical for each case yet pushed farther apart with increasing bandwidth. The channel can therefore be flexibly defined to support the modulation format and baud rate of choice. Note that ~4 dB of the MDL are attributed to the swept laser measurement system (measured by bypassing the switch), which originate from the 3DW-MUX imperfections, the aforementioned mismatch in fiber types, and various additional fiber splices, though the measurement system cannot distinguish the specific contribution of the WSS.

Next we encoded the entire C-band with an odd and even channel selection pattern, for channel bandwidths of 100, 75, 50, and 25 GHz (Fig. 5(D)–5(G)). We show the eigenvalue spread by plotting only the best and worst performing values (max-min) as well as the average IL. The clear channel bandwidth is flat and reduces as the channel spectrum assignment decreases. The WSS performance remains the same across the C-band, as witnessed by the identical performance for each WDM channel.
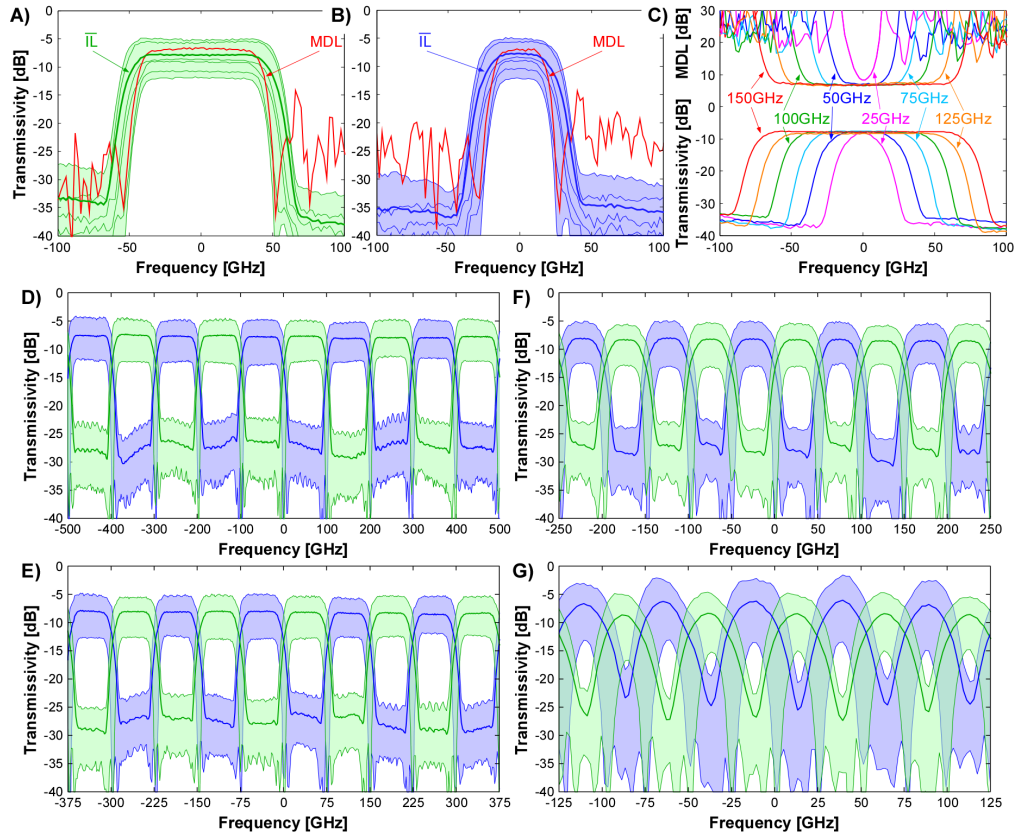
Fig. 5. Spectral performance of FMF-WSS. Single channel selection of (A) 100 GHz, and (B) 50 GHz, showing the six eigenvalue powers, the average IL, and the MDL. (C) Average IL and MDL for different flexibly defined channel bandwidths varying from 25 GHz to 150 GHz. The MDL is always narrower than the IL curve, thus defining the clear channel bandwidth. The communication band encoded with an odd/even channel selection pattern for (D) 100 GHz, (E) 75 GHz, (F) 50 GHz, and (G) 25 GHz channel bandwidth.

Lastly, we characterized the average IL and excess MDL of the FMF-WSS for the different output ports by applying different blazed phase diffraction patterns on the LCoS WSS to diffract the beam at the proper switching angle. The measurements, obtained within the clear channel bandwidth, are shown in Table 3. We subtracted from the swept-wavelength interferometer measurements the measurement system's baseline MDL of 4 dB, in order to obtain an estimate of the FMF-WSS MDL. It is not possible to determine the MDL originating from the switch alone, hence the WSS MDL could possibly be larger. Performance at the central ports achieved the best switching characteristics with less than 6 dB IL and less than 3 dB excess MDL. Both IL and excess MDL increased monotonically for the more extreme ports. While we expect a reduction in diffraction efficiency for larger beam steering angles (max diffraction angle of ArcTan(5×1.25 mm/150 mm) = 2.4°, which corresponds to an LCoS blazed grating period of 4.65 pixels) [18], this does not explain the increase in excess MDL. We believe the increased excess MDL at higher diffraction angles may come from the LCoS flyback phenomena (the phase wrapping from 2π back to zero), which introduces spatial distortions onto the beam (that are converted to amplitude modulation). This spatial distortion impacts the individual modes differently due to their structure, hence increasing MDL, whereas in SMF switching it is only an additional source of diffraction efficiency reduction (contributing to IL only).

Table 3. Insertion loss and excess mode-dependent loss measurements (in dB) for all 9 output ports of the few-mode fiber wavelength-selective switch.

Port Nr.	1	2	3	4	5	6	7	8	9
IL (dB)	8.5	7.5	6.9	5.8	5.6	6.2	6.3	7.6	9.0
Excess MDL (dB)	7.1	4.4	3.4	2.8	2.5	3.3	3.7	4.2	6.7

4. WDM transmission experiments with the FMF-WSS

To study the switch's impact on optical transmission, we built a recirculating loop to emulate cascaded switches as encountered in optical network systems. The setup is shown in Fig. 6. The test signal was an electronically precompensated 30-GBaud quadrature phase-shift keyed (QPSK) signal, which is polarization- and mode-multiplexed into a FMF using delays of 500-ns for polarization, and 50 and 100-ns between modes, respectively (equivalent to a line rate of 360 Gbps per wavelength channel). Additionally, the signal is wavelength-division multiplexed with a channel spacing of 100 GHz. We loaded either 5 or 32 wavelength channels within the C-band, generated by distributed feedback lasers (DFB), as well as two external cavity lasers (ECLs), for the channel under test and the local oscillator (LO). The recirculating loop contains single mode amplifiers, splitters and loop switches, and the signals were detected using polarization-diversity coherent receivers (PD-CRx), and captured on a 12 channels digital storage oscilloscope (DSO). Digital signal processing was performed offline.

The loop span consisted of 30-km graded-index differential group-delay compensated FMF supporting 3 spatial modes (6 when counting polarization modes [19]). The three modes were multiplexed into the transmission fiber using the 3DW-MUX, and the modes were demultiplexed after the FMF-WSS using a photonic lantern spatial multiplexer (PL-MUX) [20, 21]. The graded-index transmission fiber was attached via physical contact connectors to the step index FMF of the WSS, which again introduce MDL due to the mode size mismatch (transmission fiber's LP_{01} effective area of 68-μm^2). To minimize the effect of nonlinearities, the input power into the FMF span was kept below -3 dBm per wavelength channel.
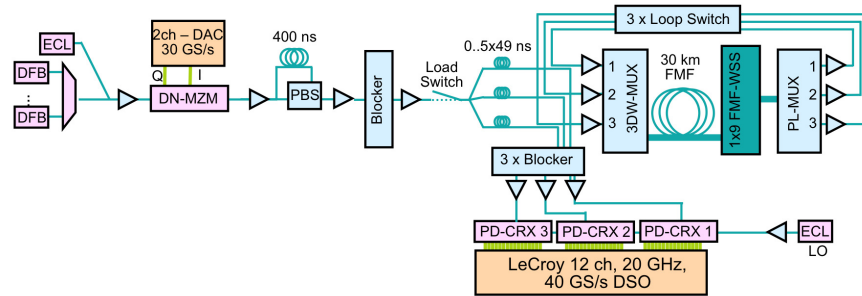

Fig. 6. Recirculating loop setup for transmission through wavelength-selective switch (EDFAs are denoted by triangles).

To measure the impact of the mode-dependent passbands we transmitted five 30-Gbaud QPSK WDM channels into the loop with the switch programmed to passband widths ranging between 25 to 100 GHz. The channel spacing was maintained at 100 GHz. Figure 7(a) shows the Q factor versus the number of switch traversals, where the Q factor was calculated from the bit-error rate (BER) recovered by off-line MIMO DSP. As reference, the performance of the loop with an equivalent loss but without the switch was measured to be Q > 13.8 dB up to 10 loops.

For passband widths of 75 to 100 GHz, good performance (above the FEC threshold) is observed up to 10 loop passes, with a performance degradation of 1 dB/pass. In this case, the performance is not limited by passbanding effects but by the MDL introduced by the switch. The performance is maintained also for lower passbands down to 62.5 GHz, where the

additional MDL introduced at the edges of the passband degrades the signal. These measurements confirm the good performance of the switch when operated at 30 Gbaud and a channel spacing of 100 GHz. The MDL of the system was also calculated based on a channel estimation and a system wide MDL degradation of 0.4 dB/pass was observed, also indicating the good performance of the WSS.

In order to confirm that the device was fully supporting extended wavelength ranges, we tested the switch with a 32 channel WDM signal, where we also made use of the attenuation capability of the switch, in order to compensate for the spectral gain tilt of our loop amplifiers. The attenuation capability was implemented by superimposing a high spatial frequency binary phase gratings in the beam steering direction on top of the blazed phase grating used for steering (a checkerboard pattern [18] resulted in high MDL values). Figure 7(b) shows the WDM results, indicating that Q > 7.7-dB can be achieved for all 32 WDM channels with up to 6 traversals of the WSS, and that the transmission distance is not limited by the WSS but by the noise build-up in the loop, due to the limited output power of our loop amplifier. This was also confirmed by monitoring the OSNR degradation.
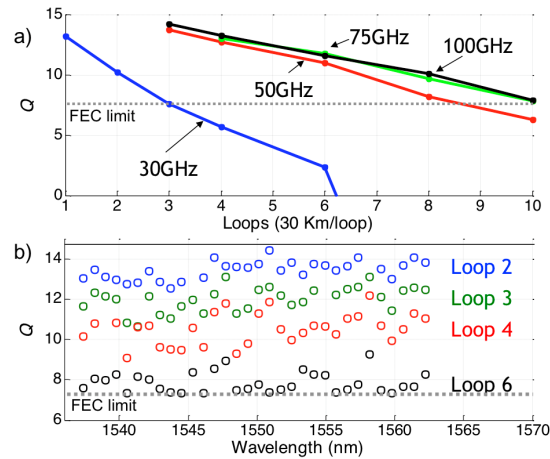

Fig. 7. a) Transmission performance as function of programmed passband after multiple switch traversal. b) Transmission results for 32 channel WDM experiment.

5. Conclusions

The theory and first realization of a WSS incorporating FMF at its input/output ports and operating internally with beams carrying several spatial modes was reported. Various sources of MDL were identified, including the impact of imperfect optical arrangement and at channel edges, the latter being an intrinsic property of this type of switch. The impact of channel bandwidth reduction due to MDL at channel edges can be reduced by designing the WSS to have finer optical resolution (requiring either larger spatial dispersion or smaller focused spot size). The switch was realized with a FMF supporting three spatial modes (LP_{01}, $2 \times LP_{11}$), and demonstrated its feasibility in transmission loop experiments. Guidelines for a FMF-WSS supporting six spatial modes were provided (LP_{01}, $2 \times LP_{11}$, $2 \times LP_{21}$, LP_{02}), which are easily extendable to higher mode counts using the Hermite-Gaussian beam approximation for the fiber modes.

The integration of FMF directly into the WSS fabric advantageously allows for identical network switching node implementations as occurring in today's in SMF-based systems. Optical networks typically require WSS with high port counts, which are feasible with a FMF-WSS, as demonstrated here with 1 × 9 functionality. However, the FMF-WSS exhibits wider channel transitions, which increases with spatial mode counts, thereby requiring larger spectral guard bands between DWDM channels and eventually reducing the wavelength-channel count. The overall carried capacity is still greatly enhanced, as the capacity gain by an

increasing mode count outweighs the capacity loss by a decreasing WDM channel count. Note that the spectral guard band can be reduced by designing the FMF-WSS with finer spectral resolution, but this requires larger optics and more demanding opto-mechanical design. Alternatively, the use of external mode demultiplexers and joint-switching with a single SMF-WSS having a high mode count can be used, which will not exhibit the requirement for enlarged spectral guard bands. However, the SDM port count is greatly reduced (by the spatial mode count) so networking functionality is impacted. One may modify the former arrangement and replace the joint-switching WSS with a WSS array, all operating in unison with each WSS handling one spatial mode. This would provide both high WDM channel density and support high port counts, but also disadvantageously increase the cost, space requirement and power consumption of its implementation linearly with the mode count, counter to the savings argument behind the SDM proposition.

Acknowledgments